KAVLI SUMMER PROGRAM IN ASTROPHYSICS

Final Report

Title: Optimal Averaging for Time-Distance Helioseismology

Abbas Raboonik

Supervisors: Aaron Birch

Damien Fournier

Laurent Gizon

7 Nov 2021

1 Introduction

The solar meridional circulation is an axisymmetric poloidal flow with velocity amplitudes ranging from 10 to 20 m s^{-1} confined to the convection zone (Hathaway and Rightmire, 2010). It arises due to an imbalance between Reynolds stresses and buoyancy forces, which are in turn sustained by convection and differential rotation (Charbonneau, 2005). Its velocity field and geometry set the strength of the polar magnetic field of the Sun and the sunspot activity over a solar cycle (Hathaway and Rightmire, 2010). Thus, understanding this phenomenon as a means of latitudinal transport of heat, angular momentum, and magnetic fields can help to better understand and constrain existing dynamo models.

In fact, the meridional circulation has become an integral part of many dynamo models today, where it is either directly incorporated in, or produced by the model (Hathaway, 1996). For example, the Babcock-Leighton dynamo theory utilizes the meridional circulation to explain the poleward transport of the surface magnetic field, and the equatorward migration of sunspots as seen in butterfly diagrams (Hathaway, 1996; Dikpati and Charbonneau, 1999). In other three-dimensional models of the dynamics of rotating convection zones such that of Glatzmaier and Gilman (1982), a poleward meridional circulation is generated by the model.

However, despite numerous endeavors, we have not yet reached a coherent picture of the meridional flow in that many studies over the years have come to conflicting conclusions. The reason for such inconsistencies and disagreements is attributed to the flow's weak velocities relative to other more dominant motions such as granulation and super-granulation. This renders the task of isolating the meridional flow signal from that of other sources taxing and to some degree inaccurate. Based on helioseismologic observations of two years of SDO data, the results of Zhao et al. (2013) suggest that the solar meridional flow has a double-cell structure, with photospheric poleward velocities of about 15 m s^{-1} and subsurface equatorward velocities of $\sim$ 10 m s^{-1}. On the other hand, based on time-distance helioseismologic analysis of two solar cycles from 1996-2019, Gizon et al. (2020) find that the meridional circulation is a single-cell in each hemisphere.

This project is a continuation of Gizon et al. (2020), where we wish not only to improve on some aspects of the previous approach, but to grasp a better understanding of possible links between time-distance helioseismology and helioseismic holography. This will be discussed in detail after we explain what we mean by optimally averaged time-distance helioseismology.

2 Method and Mathematics

In this section, we present a precis on the principles of time-distance helioseismology and lay out its core equations. Next, a model of the meridional flow involving a stream function will be discussed, and employed to infer the flow's

subsurface velocity field.

2.1 Time-distance helioseismology

Figure 1 depicts a schematic of the problem of concern in time-distance helioseismology. The objective of time-distance helioseismology is to link an acoustic wave's observed travel time τ_i to the underlying physical properties of the solar interior q^α. Here, α represents any quantity of interest (e.g., internal sound speed, velocity field), and τ_i is the time taken by the wave to travel some distance Δ_i on the photosphere between two points $\boldsymbol{x}_1$ and $\boldsymbol{x}_2$. The subscript i represents the index of a datapoint in the observational data. In the case of the meridional circulation, which is a 2D problem, it suffices to label a datapoint with the distance $\Delta_i = |\boldsymbol{x}_2 - \boldsymbol{x}_1|$ and the location of the midpoint $\lambda_i = \theta(\Delta_i/2)$, where θ is often measured in latitude (see the bottom panel of Figure 1).

Travel times can be extracted from observation using the cross-correlation function of signals. Suppose two time series $\Phi(\boldsymbol{x}_1; t)$ and $\Phi(\boldsymbol{x}_2; t)$ have been recorded over an observation period T, where Φ is a physical quantity observed at the photosphere (e.g., line-of-sight velocity data provided by Dopplergrams). Then the cross-correlation of the signals can be formed by the following integral,

$$C(\boldsymbol{x}_1, \boldsymbol{x}_2; t) = \frac{1}{T} \int_0^T \Phi(\boldsymbol{x}_1; t')\Phi(\boldsymbol{x}_2; t' + t)\, dt', \tag{1}$$

where t is called the lag time. A peak in C corresponds to the detection of identical patterns existing in both signals, indicating that a wave already observed in, say, $\Phi(\boldsymbol{x}_1; t)$ has been reobserved in $\Phi(\boldsymbol{x}_2; t)$. Then, various methods can be used to relate the lag time t to travel times τ (see e.g., Roth et al., 2007).

Figure 2 shows the cross-correlation function of SDO Dopplergrams with a cadence of 45 s observed over 8 days, after applying various spatial and temporal averaging methods to eliminate the background noise inherent to the stochastic photospheric motions. We can number each ridge by the order of its appearance n from bottom to top, starting with $n = 0$ to identify the bottom-most ridge. Then, each ridge identifies an ensemble of surface waves that ricochet off the internal surface n times at locations other than $\boldsymbol{x}_1$ and $\boldsymbol{x}_2$ before arriving at $\boldsymbol{x}_2$. For instance, the first ridge corresponds to the waves that travel directly from $\boldsymbol{x}_1$ to $\boldsymbol{x}_2$, while the second ridge is associated with all the waves that first bounce off the surface at some location other than $\boldsymbol{x}_2$ before reaching the destination.

The key idea of time-distance helioseismology is that since a wave interacts with the internal material through its journey, its travel time contains useful information about the convection zone (Gizon and Birch, 2005). Once the observed travel times are known, the central task of time-distance helioseismology is broken down into the forward, and inverse problems, which we discuss below.

2.1.1 The forward problem

To formulate the relationship between τ_i and q^α, one needs to adopt an existing solar model wherein the $\bar{\tau}_i$ and $\bar{q}^\alpha_{\text{model}}$ are known. Then, the difference between

the observed and model's travel times $\delta\tau_i = \tau_i - \bar{\tau}_i$ can be linked to a small perturbation in the $\delta q^\alpha = q^\alpha - \bar{q}^\alpha$ of the model through the linear relation (Hughes et al., 2007)

$$\delta\tau_i = \sum_\alpha \int \delta q^\alpha(\boldsymbol{r}) K_\alpha(\boldsymbol{r})\, dv, \tag{2}$$

where the integral is over the volume (or surface area in 2D) of interest, K_α is known as the sensitivity kernel for quantity α, and the summation is over all the quantities to be inferred from the data. Equation 2 is known as the forward problem. The kernels prescribe the degree to which the model is locally sensitive to a small perturbation in q_α at position $\boldsymbol{r}$, and may be derived by Born or Rytov approximations (see Birch and Kosovichev, 2000).

2.1.2 The inverse problem

Once the $\delta\tau_i$ and K_α are known, an inversion technique is employed to infer δq^α from observation. In this study, we focus our attention only to two popular and powerful inversion techniques known as "Regularized Least Squares" (RLS) used by Gizon et al. (2020), and "Subtractive Optimally Localized Averages" (SOLA).

RLS and SOLA both aim to minimize a quadratic cost function subject to specific regularization constraints. However, the core distinction between the two methods lie in the global treatment of the optimization problem in RLS, and the local treatment of SOLA.

The RLS method In RLS, the optimization task aims at minimizing a cost function under certain constraints. The constraints are fed into the minimization process through a regularization matrix denoted by D_α chosen by *a priori* considerations about the nature of the problem. Thence, given the vector of travel times τ, the sensitivity kernels K_α, and a covariance (or noise) matrix Λ encapsulating the inherent noise in the data (see Gizon and Birch, 2004, for a discussion of noise covariance), the cost function of interest in RLS is define by

$$\|\Lambda^{-1/2}\left(K_\alpha \delta q^\alpha - \tau\right)\|^2 + \lambda \|D_\alpha \delta q^\alpha\|^2, \tag{3}$$

in which $\|.\|$ is the L^2 norm. Here, λ is a scalar variable known as the regularization parameter, which together with δq^α are the unknowns of the problem. The parameter λ is determined *a posteriori* through comparison of the results with some test cases obtained from synthetic data (Gizon et al., 2020). It is evident that minimizing this function yields a "global" solution to the optimization problem.

The SOLA method On the other hand, in SOLA we seek to find local solutions that minimize a quadratic function known as the cost function at a given target point $\boldsymbol{r}_0$. The minimization process in SOLA is done in relation

with a given target function (usually taken to be the Gaussian function), whose role is to impart a certain mean behavior to the sensitivity kernel specific to the target location $\boldsymbol{r}_0$. Unlike RLS which directly solves for δq^α, the objective of SOLA is to find appropriate weighting coefficients $c_i^\alpha(\boldsymbol{r}_0)$ at a given target point $\boldsymbol{r}_0$ such that

$$\int \bar{K}(\boldsymbol{r}, \boldsymbol{r}_0, \boldsymbol{c}^\alpha)\, d\boldsymbol{r} = 1, \tag{4}$$

where the integrand is called the "averaging kernel" defined by

$$\bar{K}(\boldsymbol{r}_0, \boldsymbol{r}, \boldsymbol{c}^\alpha) = \sum_{i \in \Gamma} c_i^\alpha(\boldsymbol{r}_0) K_i^\alpha(\boldsymbol{r}), \tag{5}$$

in which Γ is the set of all the pairs $(\boldsymbol{x}_1, \boldsymbol{x}_2)$ in the data. The idea behind SOLA in time-distance helioseismology is to cut off the contribution of the data far from the target (measurement) point $\boldsymbol{r}_0$. For instance, when inferring the velocity of the meridional flow at a location in the upper hemisphere, we *a priori* expect that no information (data) from the lower hemisphere should leak into the solutions. This locality of the solutions which adds to the robustness of the method is encoded in the weighting coefficients $c_i^\alpha(\boldsymbol{r}_0)$. Figure 7 illustrates this point, where the weighting coefficients plotted in the left panel are such that the resulting averaging kernel ends up reshaping into a new local sensitivity kernel that is now only sensitive to the information around the target point.

2.2 Forward problem for the meridional circulation

As mentioned before, the meridional circulation is a 2D flow with a velocity field made up of a radial and a polar component, i.e., $\boldsymbol{U} = (U^r, U^\theta)$. The aim is to infer the subsurface velocity field from the travel time data τ_i of Gizon et al. (2020). The forward problem for $\boldsymbol{U}$ associated with a particular mid-point latitude and distance $i = (\lambda, \Delta)$ is given by

$$\tau_i = \int_0^\pi \int_{r_\mathrm{b}}^{R_\odot} \boldsymbol{K}_i \cdot \rho \boldsymbol{U}\, r \sin\theta\, dr\, d\theta, \tag{6}$$

where $\boldsymbol{K}_i = (K_i^r, K_i^\theta)$ is the sensitivity kernel vector associated with the velocity field. Figure 3 depicts the sensitivity kernel components for a specific data point corresponding to $\Delta_i = 30°$, $\lambda_i = 10°$.

Previously, Gizon et al. (2020) directly solved for $\boldsymbol{U}$ by imposing the boundary conditions that confine the flow to the convection zone, and the conservation of mass principle through additional constraints in the RLS problem.

In this study, however, we will instead solve for the stream function ψ that generates the velocity field $\boldsymbol{U}$. This has the advantage of meeting the mass conservation requirement by default. Additionally, setting up the boundary conditions for ψ can be directly implemented without a need to add further constraints in the inverse problem.

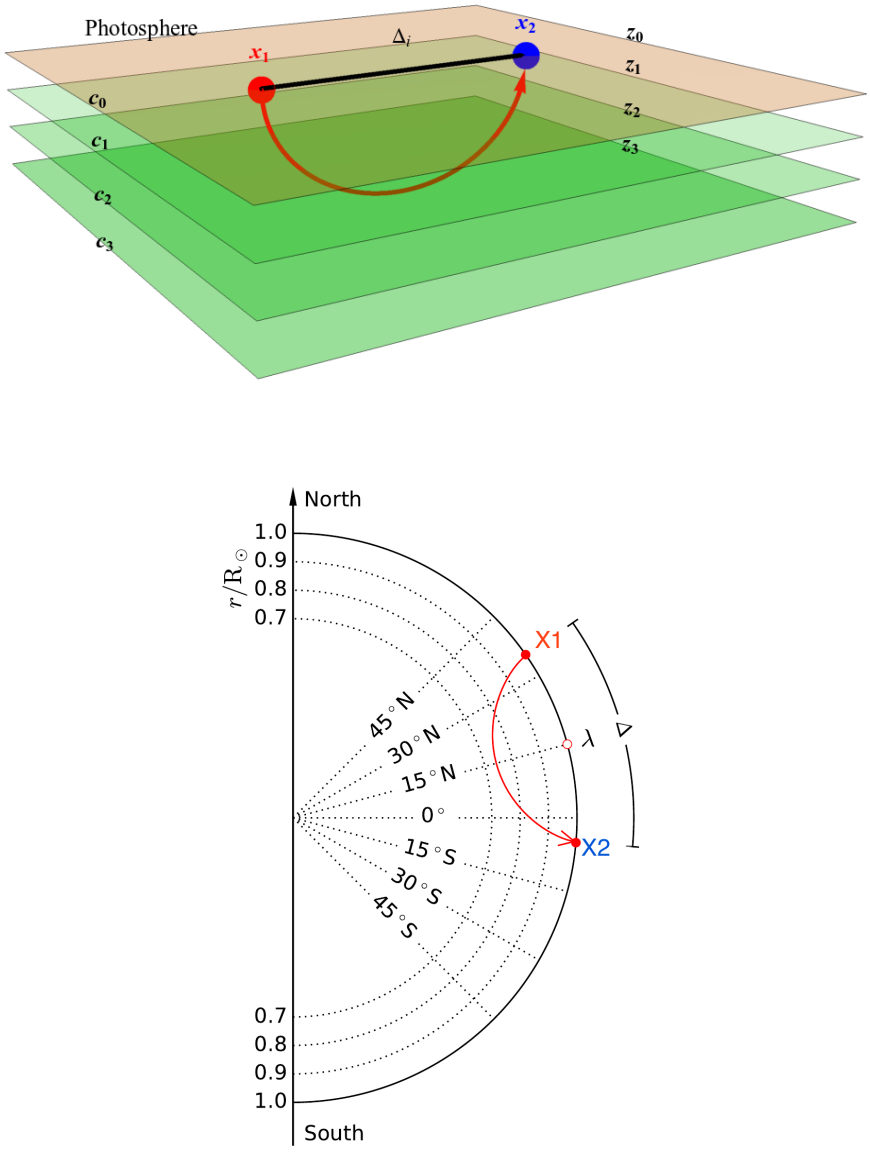

Figure 1: Schematic diagrams in (top) 3D and (bottom) 2D perspectives of the time-distance helioseismologic model of the meridional flow. An acoustic ray (shown by the red arrows) observed at $\boldsymbol{x}_1$ travels through the solar interior and, thanks to the stratification of the convection zone, reflects back to the surface at some other point $\boldsymbol{x}_2$.

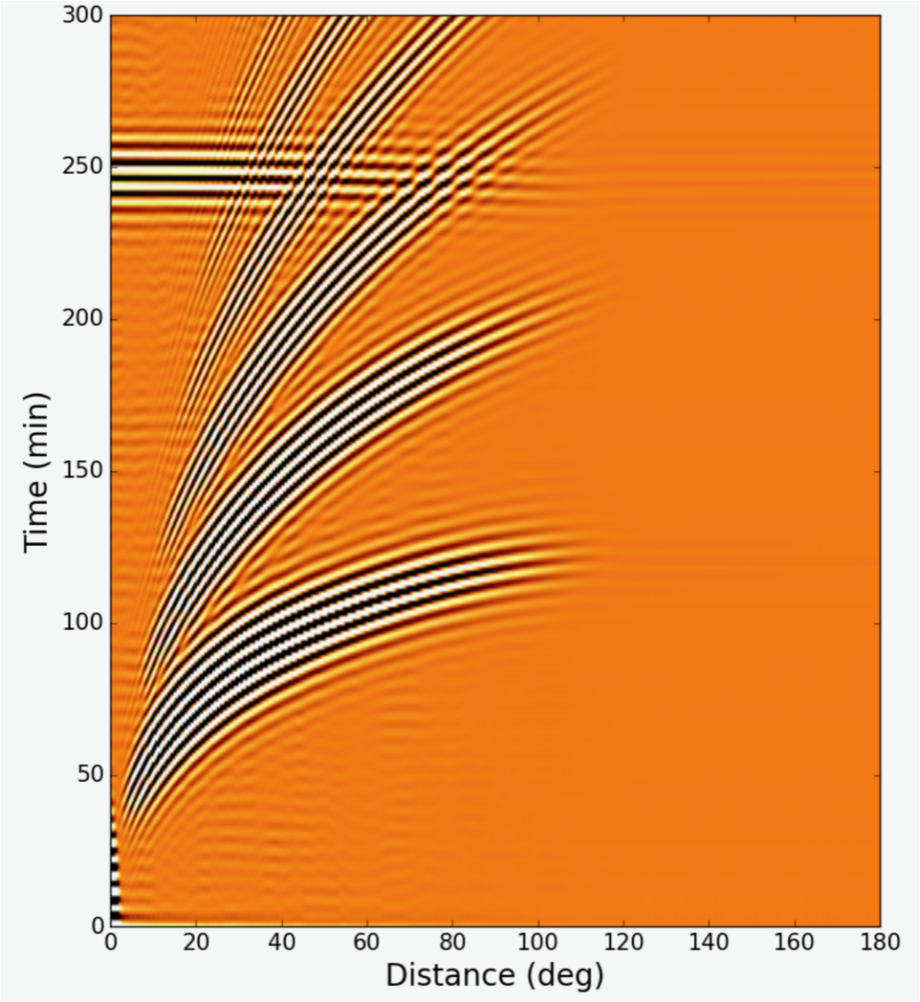

Figure 2: The cross-correlation function corresponding to 8 days worth of Dopplergram data obtained from the Solar Dynamic Observatory at a cadence of 45 s. Courtesy of Chris Hanson (NYU Abu Dhabi).

To do so, we notice that the incompressibility inherent to the meridional flow can be directly imposed by expressing the mass flux in terms of ψ prescribed in the spherical coordinate system (r, θ, φ) as follows

$$\rho \boldsymbol{U} = \boldsymbol{\nabla} \times \left(\hat{\boldsymbol{\varphi}} \frac{\psi}{r \sin \theta} \right) = \hat{\boldsymbol{r}} \frac{\partial_\theta \psi}{r^2 \sin \theta} - \hat{\boldsymbol{\theta}} \frac{\partial_r \psi}{r \sin \theta}, \tag{7}$$

where $\hat{\boldsymbol{r}}$, $\hat{\boldsymbol{\theta}}$, and $\hat{\boldsymbol{\varphi}}$ are respectively the radial, polar, and azimuthal unit vectors. Substituting this in Eq. (6) gives

$$\tau_i = \int_0^\pi \int_{r_b}^{R_\odot} \frac{K_i^r \, \partial_\theta \psi}{r} \, dr \, d\theta - \int_0^\pi \int_{r_b}^{R_\odot} K_i^\theta \, \partial_r \psi \, dr \, d\theta, \tag{8}$$

Performing integration by parts yields

$$\tau_i = \int_{r_\mathrm{b}}^{R_\odot} \frac{1}{r} \left[\int_0^\pi \partial_\theta \left(K_i^r \, \psi \right) \, d\theta - \int_0^\pi \psi \, \partial_\theta K_i^r \, d\theta \right] dr \\ - \int_0^\pi \left[\int_{r_\mathrm{b}}^{R_\odot} \partial_r \left(K_i^\theta \, \psi \right) \, dr - \int_{r_\mathrm{b}}^{R_\odot} \psi \, \partial_r K_i^\theta \, dr \right] d\theta. \tag{9}$$

This can be further simplified by imposing appropriate boundary conditions. At the radial boundaries ($r = r_\mathrm{b}$, $R_\odot$), we expect no flow entering or escaping the system. To meet these requirements, we must choose $U^r \propto \partial_\theta \psi = 0$. At the polar boundaries ($\theta = 0, \pi$), the flow must be radial and vanish at the radial boundaries. Selecting $U^\theta \propto \partial_r \psi = 0$ at $\theta = 0$ and $\theta = \pi$ meets these constraints. Committing the boundary conditions, Eq. (9) can be re-written as

$$\tau_i = \int_0^\pi \int_{r_\mathrm{b}}^{R_\odot} \psi \left[\partial_r K_i^\theta - \frac{\partial_\theta K_i^r}{r} \right] dr \, d\theta + C_i, \tag{10}$$

where C_i are given by the BCs according to

$$C_i = \left[\psi \int_{r_\mathrm{b}}^{R_\odot} \frac{K_i^r}{r} \, dr \right]_0^\pi - \left[\psi \int_0^\pi K_i^\theta \, dr \right]_{r_\mathrm{b}}^{R_\odot}. \tag{11}$$

However, ψ is any continuous function satisfying the BCs, and hence, can be chosen to vanish identically at the boundaries. Note that this is not a superfluous boundary condition, but merely a simplifying restriction on the freedom of choice of ψ. Thereby, $C_i = 0$ and we arrive at the final form of the forward problem for the stream function,

$$\tau_i = \int_0^\pi \int_{r_\mathrm{b}}^{R_\odot} \mathcal{K}_i \psi \, dr \, d\theta, \tag{12}$$

where $\mathcal{K}_i$ is the modified sensitivity kernel for the stream function ψ given by

$$\mathcal{K}_i = \partial_r K_i^\theta - \frac{\partial_\theta K_i^r}{r}. \tag{13}$$

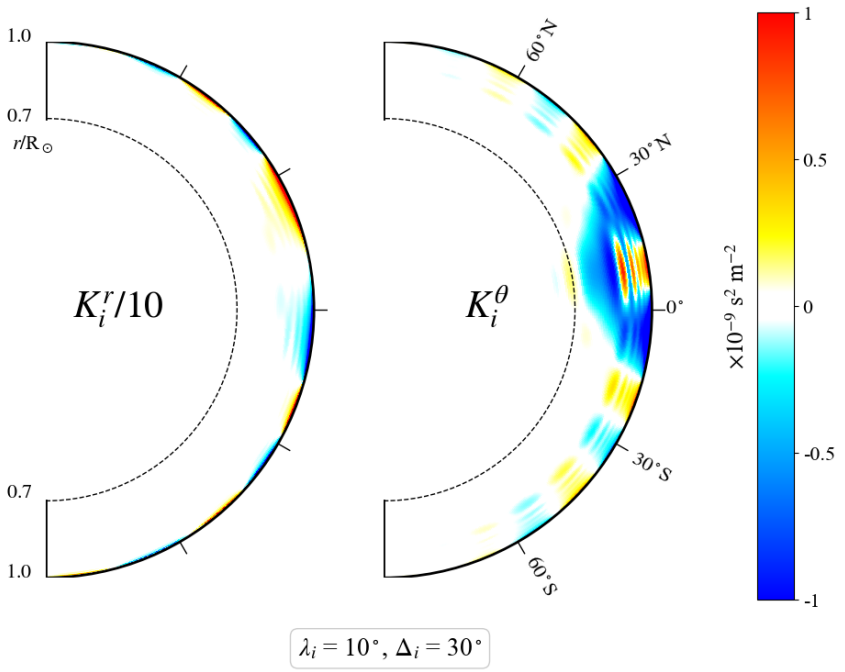

Figure 3: The radial and polar components of the sensitivity kernel used by Gizon et al. (2020). Shown as an illustrative example, the plot corresponds to the specific center location λ_i and the separation distance Δ_i as labeled.

2.3 Inverse problem

As mentioned before, the averaging sensitivity kernel for ψ can be defined by

$$\begin{aligned}\bar{\mathcal{K}}(\boldsymbol{r}_0, \boldsymbol{r}, \omega, \boldsymbol{c}) &= \sum_{i\in\Gamma} c_i(\boldsymbol{r}_0)\mathcal{K}_i(\boldsymbol{r}, \omega) \\ &= \boldsymbol{c}\cdot\boldsymbol{\mathcal{K}},\end{aligned} \tag{14}$$

where Γ is the set of all the rays associated with the observed waves, and $\boldsymbol{r_0}$ is a target point at which we wish to infer the value of ψ, and c_i are the weighting coefficients. In order to obtain statistically cogent results, the averaging kernel is required to normalize to unity, hence

$$\int \bar{\mathcal{K}}(\boldsymbol{r}_0, \boldsymbol{r}, \omega, \boldsymbol{c})\, d\boldsymbol{r} = 1. \tag{15}$$

The SOLA problem for a single real-valued averaging sensitivity kernel takes the following form

$$\begin{aligned}\mathcal{L}(\boldsymbol{c}, \mu) = \int \left|\bar{\mathcal{K}}(\boldsymbol{r}_0, \boldsymbol{r}, \omega, \boldsymbol{c}) - \mathcal{T}(\boldsymbol{r}_0, \boldsymbol{r})\right|^2 d\boldsymbol{r} + \lambda \sum_{i,j\in\Gamma} c_i(\boldsymbol{r}_0)E_{ij}c_j(\boldsymbol{r}_0) \\ + \mu\left[\int \bar{\mathcal{K}}(\boldsymbol{r}_0, \boldsymbol{r}, \omega, \boldsymbol{c})\, d\boldsymbol{r} - 1\right],\end{aligned} \tag{16}$$

where $\mathcal{T}$ is a target function, and μ is a Lagrange multiplier, and E is the covariance matrix. $\partial\mathcal{L}/\partial\mu = 0$ simply returns the normalization constraint set out in Eq. (15). On the other hand, setting $\partial\mathcal{L}/\partial c_m = 0$ yields

$$\sum_{i\in\Gamma} c_i \underbrace{\left[\int \mathcal{K}_i\mathcal{K}_m\, d\boldsymbol{r} + \lambda E_{im}\right]}_{M_{mi}} + \frac{\mu}{2}\int \mathcal{K}_m\, d\boldsymbol{r} = \underbrace{\int \mathcal{T}\mathcal{K}_m\, d\boldsymbol{r}}_{D_m}. \tag{17}$$

The terms inside the square brackets define the elements of a $\Gamma\times\Gamma$ Hermitian matrix M. The integral on the RHS gives the elements of a $\Gamma\times 1$ column vector $\boldsymbol{D}$. We may merge Eqs. 15 and 17 into a single matrix equation by defining the following augmented matrices

$$\tilde{\boldsymbol{D}} = \begin{pmatrix}\boldsymbol{D}\\ 1\end{pmatrix}_{(\Gamma+1)\times 1} \tag{18}$$

$$\tilde{\boldsymbol{X}} = \begin{pmatrix}\boldsymbol{c}\\ \mu/2\end{pmatrix}_{(\Gamma+1)\times 1} \tag{19}$$

$$\tilde{M} = \left(\begin{array}{c|c} M & \int \boldsymbol{\mathcal{K}}\, d\boldsymbol{r} \\ \hline \int \boldsymbol{\mathcal{K}}^T\, d\boldsymbol{r} & 0\end{array}\right)_{(\Gamma+1)\times(\Gamma+1)}, \tag{20}$$

where T is means transpose. Thus, we have

$$\tilde{M}\tilde{\boldsymbol{X}} = \tilde{\boldsymbol{D}}. \tag{21}$$

Note that $\tilde{M}$ is Hermitian, and consequently invertible. As such, we may find $\tilde{\boldsymbol{X}}$ by

$$\tilde{\boldsymbol{X}} = \tilde{M}^{-1}\tilde{\boldsymbol{D}}. \tag{22}$$

Once $\tilde{\boldsymbol{X}}$, and hence $\boldsymbol{c}$ are known, the inversion process can be readily completed by finding the averaging stream function $\bar{\psi}$ through

$$\bar{\psi}_\omega(\boldsymbol{r}_0) = \int \mathcal{K}(\boldsymbol{r}_0, \boldsymbol{r}, \omega, \boldsymbol{c})\psi(\boldsymbol{r})\, dr\, d\theta = \sum_{i\in\Gamma} c_i(\boldsymbol{r}_0)\tau_i. \tag{23}$$

3 Results

Having set up the mathematical framework, here we will present the findings of the project achieved thus far. The code for all the computations is written in Python and is capable of parallel computation.

3.1 Recovering travel times from the stream function

Let us first verify the method by reproducing travel times of the previous study by Gizon et al. (2020) using the modified kernel $\mathcal{K}$ derived in Eq. (12). Figure 4 shows $\mathcal{K}$ for the same data point as Figure 3, at $\Delta_i = 30°$, $\lambda_i = 10°$.

To construct ψ, we will use the velocity profiles inferred from the 1996-2008 and 2008-2019 data sets of Gizon et al. (2020). Equation 7 can be integrated to find ψ given the velocity field components U^r or U^θ according to

$$\psi = \int_0^\pi \rho U^r r^2 \sin\theta\, d\theta, \tag{24}$$

or equivalently

$$\psi = -\int_{r_b}^{R_\odot} \rho U^\theta r \sin\theta\, dr. \tag{25}$$

Although either one of Eqs. 24 or 25 can be used to obtain the stream function directly from a velocity component (U^r or U^θ), nevertheless, in practice, certain sources of numerical error arise which may render one component more accurate and favorable. In our inferred flow models, the dominant velocity component was U^θ, and hence was used to obtain ψ from the Equation 25. Figure 5 portrays the stream function ψ (top left), the second-time reconstructed velocity components (top middle and right), and the associated errors (bottom) corresponding to the 2008-2019 data set. It is worth mentioning that in our numerical calculations, it was interestingly found that integrating from the solar surface at $R_\odot$ down to the bottom of the convection zone at r_b significantly increased the accuracy ψ. We suspect that this has to do with the fact that numerical integration is nothing but a finite summation of discrete numbers, and hence

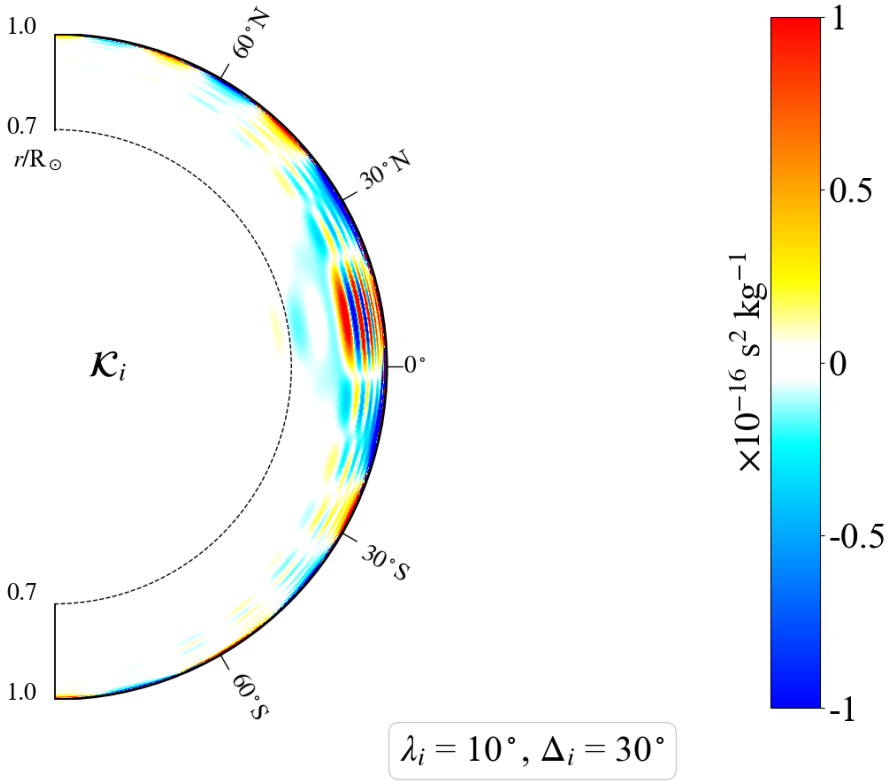

Figure 4: The modified sensitivity kernel for the stream function shown for the same combination of λ_i and Δ_i as Figure 3 for illustrative purposes.

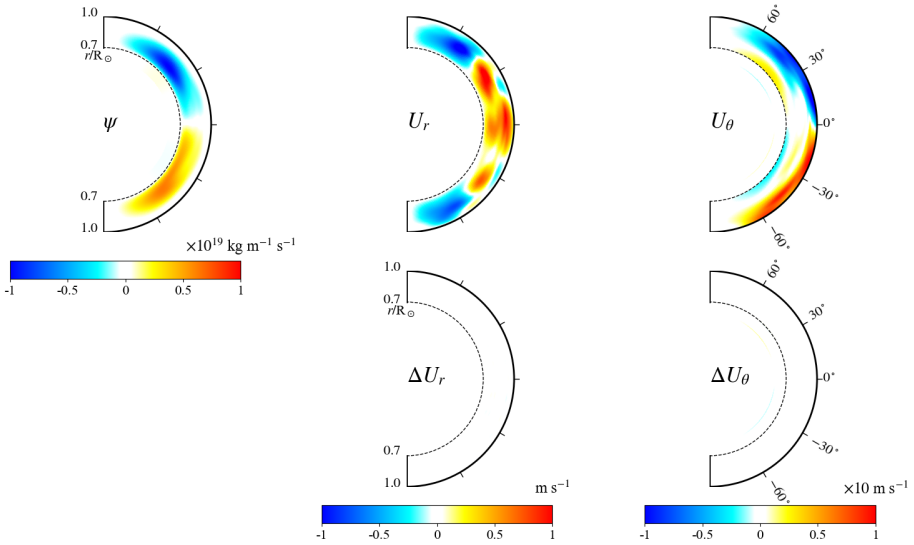

Figure 5: (Top left) The stream function ψ extracted from the inferred meridional velocity field of Gizon et al. (2020) using Eq. (25). (Top middle and right) The velocity field components back-calculated from the stream function. (Bottom) The errors associated with re-computing the velocity components from ψ.

summing from the larger values of the integrand of Eq. (25) at the solar surface down to the smaller values at the bottom of the convection zone can remarkably boost the integration precision.

With the stream function at hand, we are now able to use Eq. (12) and regenerate the travel times of Gizon et al. (2020) in a reverse process. Figure 6 depicts the scatter plot of the recovered travel times using the stream function and the modified sensitivity kernel. The matching of the regenerated travel time data and the identity line (shown in red) indicates a maximum error of less than 1%.

3.2 Recovering ψ from the averaging kernel

As one last corroborative task to test the validity of the SOLA scheme outlined in Section 2.3, we employ the modified kernel $\mathcal{K}$ and a Cartesian Gaussian target function

$$\mathcal{T}(r,\theta) = \exp\left(-\frac{(r-r_0)^2\cos^2(\theta) + (r-r_0)^2\sin^2(\theta)}{\sigma^2}\right), \tag{26}$$

to compute the mass matrix of Equation 18 and its inverse. Once M^{-1} is known, it can be used to find the averaging coefficients c_i and finally utilize them to

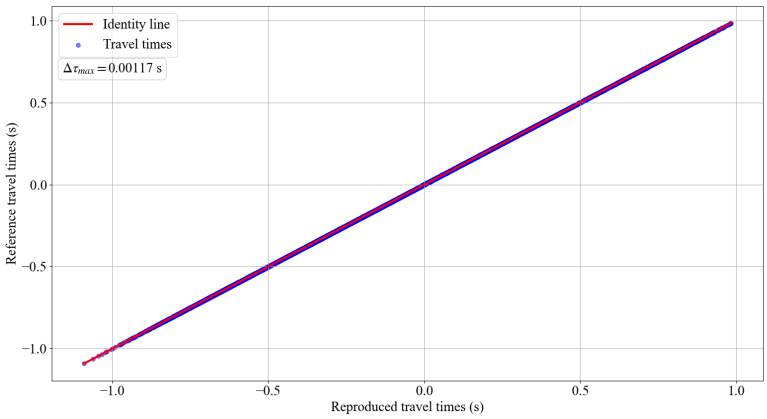

Figure 6: Scatter plot of the reference travel time (red) data of Gizon et al. (2020) versus that recovered from the stream function (blue).

invert for ψ through Eq. (23). Figure 7 depicts the scatter plot of the averaging coefficients (left), the averaging kernel (middle), and the Gaussian function used in this example (right) at the target point $r = 0.9R_\odot$ and $\theta = 40^\circ$ latitude. For this specific case, Eq. (23) yields

$$\frac{\bar{\psi}(\boldsymbol{r}_0)}{\psi(\boldsymbol{r}_0)} = 1.05, \tag{27}$$

which is a reasonable result since the previous model is expected to have more accuracy near the solar surface and a matching answer for $\bar{\psi}$ is indicative of high fidelity of the current scheme.

4 Remaining Work

For the remainder of the project, we will include

- optimal choices for target functions and other parameters
- extend the method to directly inverting cross-correlation data instead of travel times
- compare the method with other inversion schemes and helioseismology methods such as "helioseismic holography".

In particular, we are interested in learning if there is any connection at a deeper level between local inversions methods like SOLA and helioseismic holography.

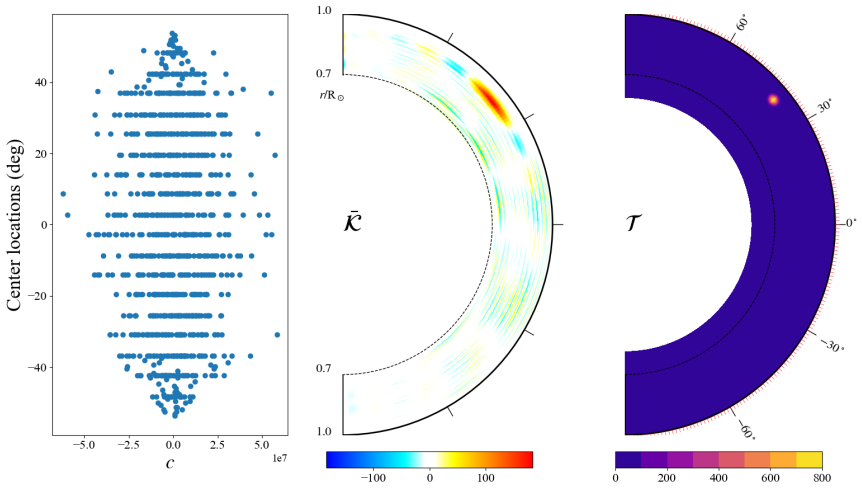

Figure 7: The weighting coefficients (left), averaging kernel (middle), and the target function (right) corresponding to the SOLA minimization problem at the target point $r_0 = 0.9R_\odot$ and $\theta = 40°$.

References

Birch, A. and Kosovichev, A. (2000). Travel Time Sensitivity Kernels. *Solar Phys.*, 192:193–201.

Charbonneau, P. (2005). Dynamo Models of the Solar Cycle. *Living Reviews in Solar Physics*, 2(1):1–83.

Dikpati, M. and Charbonneau, P. (1999). A babcock-leighton flux transport dynamo with solar-like differential rotation. *The Astrophysical Journal*, 518(1):508–520.

Gizon, L. and Birch, A. (2005). Local Helioseismology. *Living Rev. Solar Phys.*, 2(6).

Gizon, L. and Birch, A. C. (2004). Time-Distance Helioseismology: Noise Estimation. *The Astrophysical Journal*, 614(1):472–489.

Gizon, L., Cameron, R. H., Pourabdian, M., Liang, Z. C., Fournier, D., Birch, A. C., and Hanson, C. S. (2020). Meridional flow in the Sun's convection zone is a single cell in each hemisphere. *Science*, 368(6498):1469–1472.

Glatzmaier, G. A. and Gilman, P. A. (1982). Compressible convection in a rotating spherical shell. V - Induced differential rotation and meridional circulation. *Astrophys. J.*, 256:316–330.

Hathaway, D. H. (1996). Doppler Measurements of the Sun's Meridional Flow. *The Astrophysical Journal*, 460:1027.

Hathaway, D. H. and Rightmire, L. (2010). Flow over a Solar Cycle. *Science*, 327(March):0–3.

Hughes, S. J., Pijpers, F. P., and Thompson, M. J. (2007). Optimized data masks for focussed solar tomography: Background and artificial diagnostic experiments. *Astronomy and Astrophysics*, 468(1):341–351.

Roth, M., Gizon, L., and Beck, J. G. (2007). Measuring helioseismic travel times. *Astronomische Nachrichten*, 328(3-4):215–222.

Zhao, J., Bogart, R., Kosovichev, A., Duvall Jr., T., and Hartlep, T. (2013). Detection of Equatorward Meridional Flow and Evidence of Double-cell Meridional Circulation inside the Sun. *Astrophys. J. Lett.*, 774:L29.